

# **Microfabricated Membrane Mirror with Transparent Electrode for Adaptive Optics**

**Peter Kurczynski,<sup>a,b</sup> Harold M. Dyson,<sup>a,b</sup> Bernard Sadoulet,<sup>b</sup>**

**J. Eric Bower,<sup>a,c</sup> Warren Y-C. Lai,<sup>a,c</sup> William M. Mansfield,<sup>a,c</sup> J. Ashley Taylor<sup>a,c</sup>**

<sup>a</sup>Bell Laboratories, Lucent Technologies, Murray Hill, NJ 07974

<sup>b</sup>University of California Berkeley, Berkeley, CA 94720

<sup>c</sup>New Jersey Nanotechnology Consortium, Murray Hill, NJ 07974

## **ABSTRACT**

Copyright 2005

**Keywords:** adaptive optics, MEMS, micro-opto-electromechanical systems, optical MEMS, micromirrors, deformable mirrors

## **1. INTRODUCTION**

Micro-electromechanical systems (MEMS) offer a promising alternative to piezoelectric and other deformable mirror types used in adaptive optics applications.<sup>1</sup> In particular, Flexible Optical BV, formerly OKO Technologies, developed inexpensive 37 actuator membrane mirrors<sup>2</sup> that are capable of approximately 1.5  $\mu\text{m}$  single actuator stroke at 300 V. Various groups have used membrane mirrors from Flexible Optical BV for application to retinal imaging, both

correction<sup>3,4</sup> and generation of aberrations,<sup>5</sup> for application to astronomical imaging, both correction,<sup>6</sup> and generation of aberrations,<sup>7</sup> as well as for confocal microscopy,<sup>8</sup> adaptive laser wavefront correction,<sup>9</sup> and cryogenic adaptive optics intended for space based applications.<sup>10</sup>

However, previous MEMS deformable mirrors in general, and membrane mirrors in particular, have too few actuators, and/or insufficient stroke to fully correct the aberrations of human vision. Simulations suggest that atmospheric correction of very large telescope images will also require greater flexibility and more degrees of freedom than has currently been demonstrated. Until recently, the lack of availability of high density interconnects and drive electronics limited the number of actuators that could be realized in MEMS deformable mirrors to at most on the order of 100. Geometrical factors such as the membrane-electrode spacing, material factors such as the membrane stress, and other factors such as the maximum operating voltage, limited the amount of stroke that could be attained with membrane mirrors.

In this paper we demonstrate the fabrication and assembly of membranes with low stress, and consequently greater flexibility than previous designs. We measured the mechanical resonant frequencies of membranes in vacuum in order to determine the membrane stress after fabrication. We correlated the Boron impurity concentration in the silicon with the intrinsic stress, and we identified other factors in the device assembly process that impact the membrane tension.

## 2. DEVICE FABRICATION

Membranes were fabricated from essentially un-doped<sup>\*</sup>, single crystal, silicon-on-insulator (SOI) wafers with extremely low (tensile) intrinsic stress. Low stress is a desirable feature for these devices because it enables highly flexible membranes that are easily deformed. Other common membrane materials include silicon nitride (typically 50-100 MPa stress), and polycrystalline silicon (typically 50 MPa stress). Membranes were 15mm diameter circles and had 1  $\mu\text{m}$  thickness.

The transparent electrode consists of a glass window, undercoated with a transparent, electrically conductive material. This electrode is positioned above the membrane and allows an upward electrostatic pressure to be applied to the membrane. This bias pressure greatly facilitates control of the membrane shape, which is adjusted by varying the spatial distribution of voltages on the underlying electrode array.

Transparent electrode parts were machined out of Borofloat ® Borosilicate float glass by an outside vendor. Figure 2 illustrates the geometry of the parts and their fitting into the membrane device. The undersides of the parts were coated with indium tin-oxide (ITO) to a specified resistance of 500  $\Omega/\text{square}$ . These devices were intended for visible light operation, for which Borofloat ® glass and ITO each have good transmission properties. The top surfaces of the transparent electrode parts were AR coated for optimum transmission in the 400-900 nm range.

---

<sup>\*</sup> The un-doped silicon in fact had a composite structure of 0.2  $\mu\text{m}$  thickness lightly boron doped silicon ( $2.5\text{--}3 \times 10^{14} \text{ atoms/cm}^3$ ) capped with 0.8  $\mu\text{m}$  un-doped silicon. The composite structure arose from the wafer manufacturing process, whereby the initial 0.2  $\mu\text{m}$  layer was grown commercially and supplemented with an epitaxial deposition of un-doped silicon that was performed independently to increase the total thickness of the silicon to 1  $\mu\text{m}$ .

For long wavelength infra-red applications, a different choice of window material and transparent, conductive coating would be necessary; an appropriate choice of such materials has been identified for future experiments.

The transparent electrode was installed into the micro-fabricated, recessed cavity of the membrane chip. This recessed cavity supports the transparent electrode on a shelf above the membrane. This shelf height was 30-60  $\mu\text{m}$ , with chip-to-chip variation caused by variations in the silicon etch rate across the wafer, as mentioned in Section 2. The shelf height of a single chip varied around its circumference by approximately 10  $\mu\text{m}$ ; this figure suggests a deviation from parallelism between the transparent electrode and the membrane of approximately 0.001 radians = 0.06 degrees (15  $\mu\text{m}$ /15 mm).

Electrical connectivity to the ITO layer of the transparent electrode was accomplished through the vent holes. A titanium/gold layer was evaporated into the vent hole, and a small portion of the ITO layer. Subsequently, a wire was attached to the front side of the part, near the vent hole, with a small bead of conductive epoxy. This epoxy bead was allowed to penetrate slightly onto the sidewall of the vent hole, without completely penetrating through to the underside of the part. In this way, the transparent electrode was connected to an off-chip power supply or drive electronics, and the ITO layer was electrically isolated from the membrane.

### **3. CONTROL**

Operation of the mirror in closed loop is done with one of two algorithms. Each of these algorithms use a reconstructor matrix that is determined by “poke-ing” each actuator of the device and measuring the response. Subsequently, an iterative procedure is used to drive the membrane to produce either a flat wavefront, or a user specified wavefront such as a sinusoidally varying wavefront or a Zernike polynomial. The iterative procedure for driving the membrane to produce a flat wavefront is outlined in the Appendix.

The iterative procedures do not control the transparent electrode voltage. At present this voltage is set manually, causing the membrane to produce a curved wavefront, as illustrated in Figure 1(a). Subsequently, the iterative loop is closed, whereby the membrane relaxes to produce the target wavefront after a number of iterations. Typically 5-50 iterations are necessary for the wavefront to converge to a stable configuration. An adjustable gain parameter is used to prevent the membrane from entering into oscillations. Typically the iterative procedure is very sensitive to the value of this gain parameter, as well as the transparent electrode voltage, and the array voltages.

### **4. RESULTS**

#### 4.1. Flatten wavefront

In this experiment, a voltage is applied to the transparent electrode, causing the membrane to produce a highly curved wavefront. Then the iterative loop is closed, and the membrane tries to flatten itself, while under tension from the attraction to the transparent electrode. Typical transparent electrode voltages are 9-12 V. At these voltages, the wavefront deforms to  $\sim 20\text{ }\mu\text{m}$  peak to valley. The transparent electrode causes the membrane to deform in a slightly off center paraboloid, which suggests lack of parallelism between the membrane and transparent electrode.

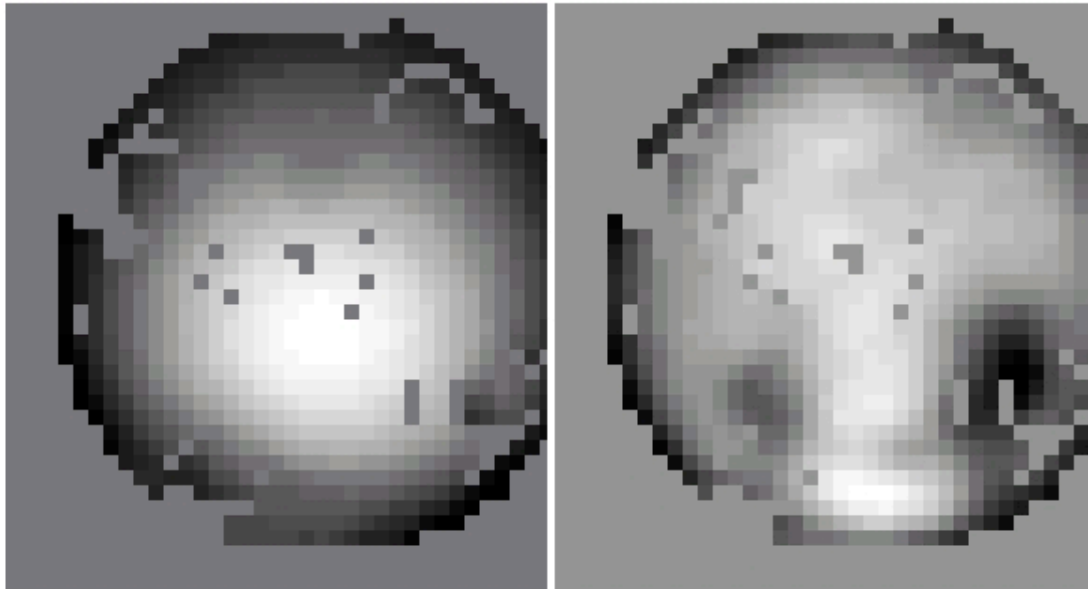


Figure 2 a,b. Before and after command to flat experiment. Left figure (a) illustrates measured wavefront resulting from 9 V applied to the transparent electrode. PV OPD is  $19\text{ }\mu\text{m}$ . Wavefront shape is an off-center paraboloid. Right figure (b) illustrates measured wavefront

resulting from closing the loop and iterating to a flat wavefront. PV OPD is 4  $\mu\text{m}$ . “West” chip side is down in the figure. “North” is to the left. Data taken on 1/13/2005.

#### 4.2 Large deformation... 20 $\mu\text{m}$

#### 4.3 Influence functions

Influence functions for the device 11-17-2004-A demonstrate the optical wavefront deformation resulting from actuation of a single electrode of the device. For the data below, a single electrode was charged to 120 V. The resulting wavefront exhibited 9  $\mu\text{m}$  peak to valley optical path difference. Each electrode is 275  $\mu\text{m}$  on a side. The array has 1024 electrodes tiling a 10 mm diameter circular region. The wavefront is 15 mm diameter, which corresponds to the membrane diameter. These data were taken on 12-20-2004. See also, the MPEG movie [SingleElectrode\\_\\_5xSteps\\_\\_9umPVOPD\\_v2.mpg](#)

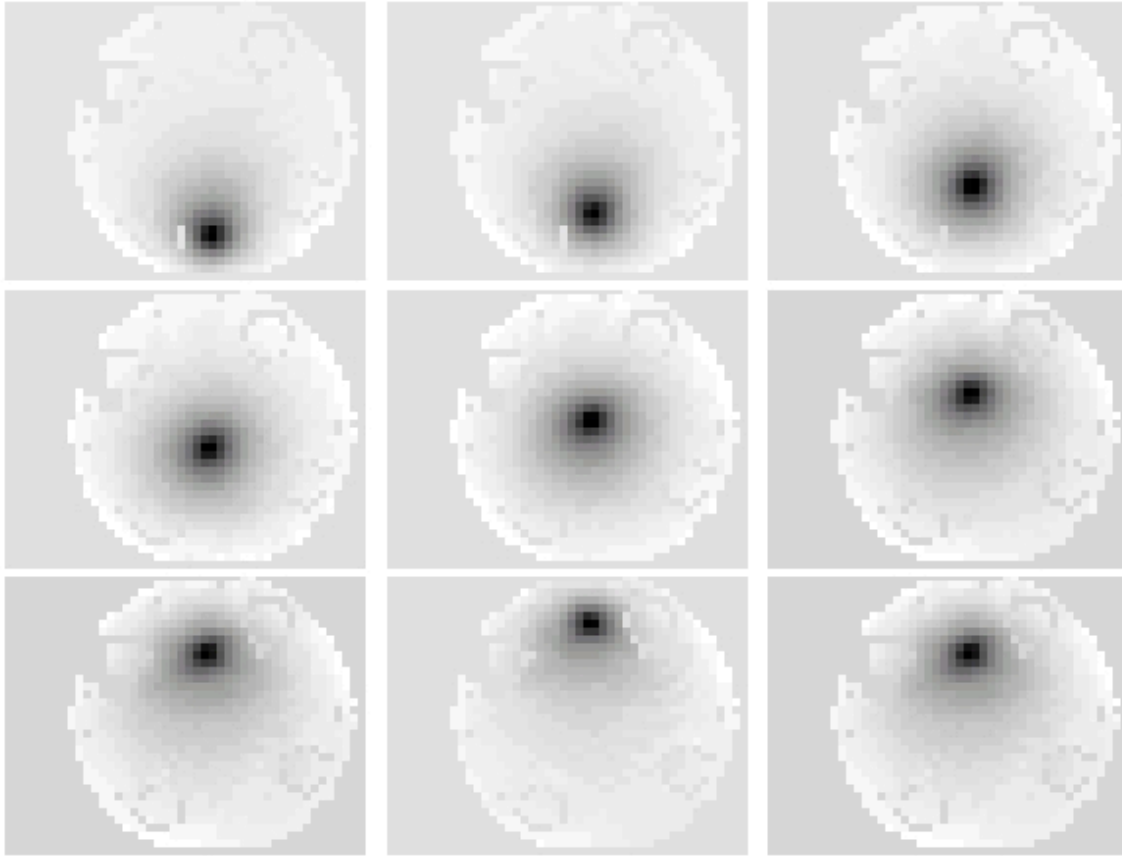


Figure 1. Representative influence functions of 1024 electrode membrane device. Each image illustrates the wavefront (optical path difference) resulting from energizing a single electrode of the array. The dark spot corresponds to a (peak to valley) deformation of 9  $\mu\text{m}$ . Operating voltage was 120 V.



Electrode binning	# binned electrodes in array (modes)	Effective electrode width, $\mu\text{m}$	Voltage reqd. for 10 $\mu\text{m}$ (optical) deflection, V
1x1	1024	275	>~120
2x2	361	550	71
3x3	169	825	40
5x5	63	1375	25
7x7	36	1925	19
16x16	9	4400	10

Table 1. Binning modes of 1024 membrane mirror and operating voltage required for 10  $\mu\text{m}$  (optical) wavefront deformation. First column indicates the number of electrodes per bin; the second column indicates the number of binned electrodes in the entire array; third column indicates the width of each electrode bin; fourth column indicates the voltage required on a single binned electrode to yield 10  $\mu\text{m}$  peak to valley wavefront deformation, with all other array voltages and transparent electrode voltage held at zero volts. In each case of single binned electrode actuation, the resulting wavefront deformation had a FWHM of approximately 3 mm.

#### 4.4 Deflection vs. voltage

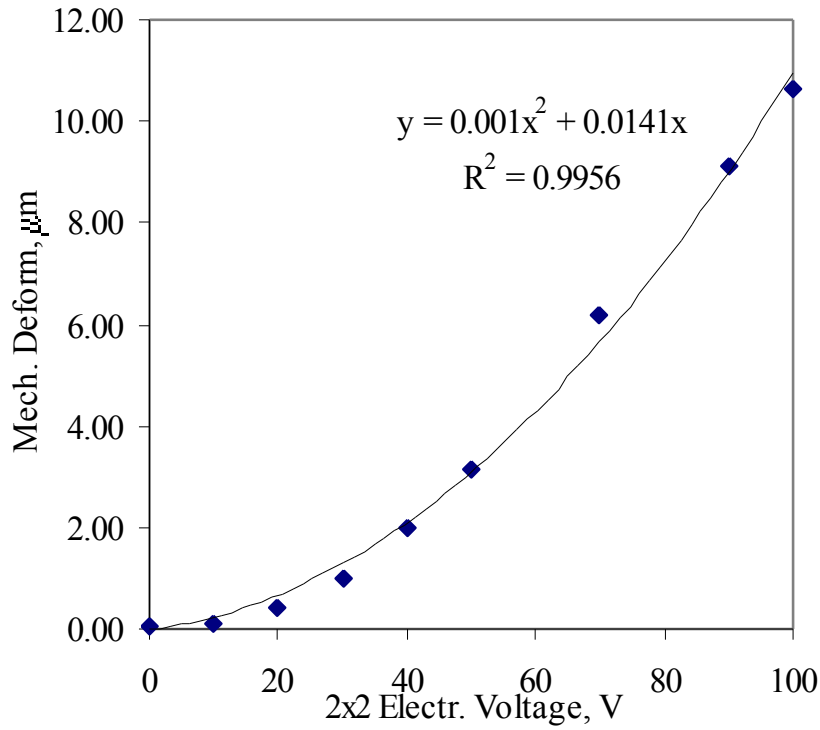


Figure 5. Deflection vs. voltage data for the membrane device operated in a 2x2 binning mode. Data points (diamonds) consist of mechanical deflections at each voltage. Mechanical deflection was inferred from the wavefront optical path difference measurements by dividing the peak to valley optical path difference for each measurement by two (due to double pass reflection). The solid line is a quadratic fit to the data, with the fit constrained to pass through the origin. The equation of the best fit line and  $R^2$  goodness of fit statistic are indicated in the figure.

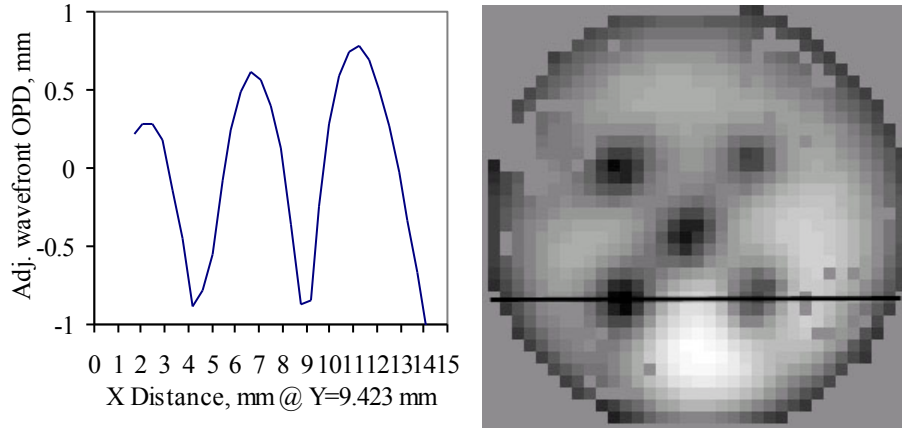


Figure 3% a,b. Left figure (a) illustrates a slice through the wavefront optical path difference data used in a 2D spatial variation pattern. A linear trend has been removed from the data for clarity. Right figure (b) illustrates the entire optical path difference data. The horizontal black line corresponds to the position of the slice through the data depicted in (a). For these data, five 2x2 electrode bins were charged to 90 V (corresponding in position to the dark spots in the figure), and the transparent electrode was charged to 13 V. Peak to valley optical path difference over the entire wavefront is 9.6  $\mu\text{m}$ .

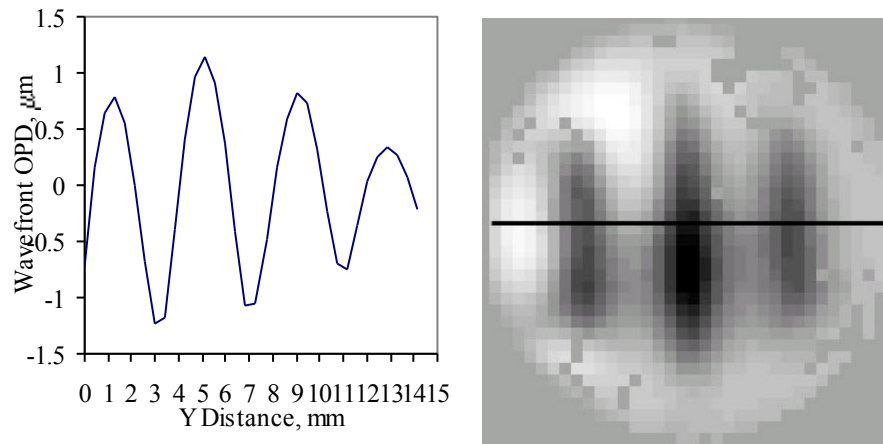


Figure 3 a,b. Left figure (a) illustrates a slice through the wavefront optical path difference data used in a 1D spatial variation pattern. An overall parabolic trend has been removed from the data for clarity. Right figure (b) illustrates the entire optical path difference data. The horizontal black line corresponds to the position of the slice through the data depicted in (a). For these data, three rows of electrodes were charged to 5, 18, 31 V respectively (corresponding in position to the vertical stripes in the figure), and the transparent electrode was charged to 11 V. Peak to valley optical path difference over the entire wavefront is 9.6  $\mu\text{m}$ .

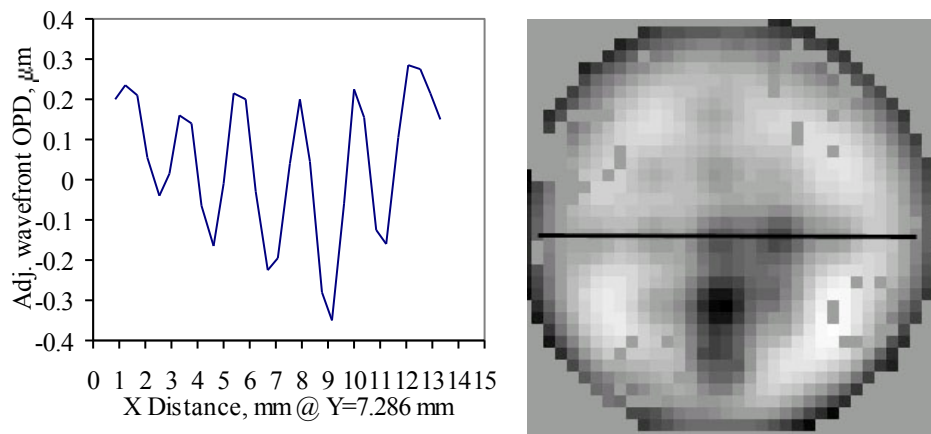


Figure 3& a,b. Left figure (a) illustrates a slice through the wavefront optical path difference data used in a 2D spatial variation pattern. A moving average trend has been removed from the data for clarity. Right figure (b) illustrates the entire optical path difference data. The horizontal black line corresponds to the position of the slice through the data depicted in (a). For these data, 13 4x4 electrode bins were charged to 44 V (corresponding in position to the dark spots in the

figure), and the transparent electrode was charged to 13 V. Peak to valley optical path difference over the entire wavefront is 10.8  $\mu\text{m}$ .

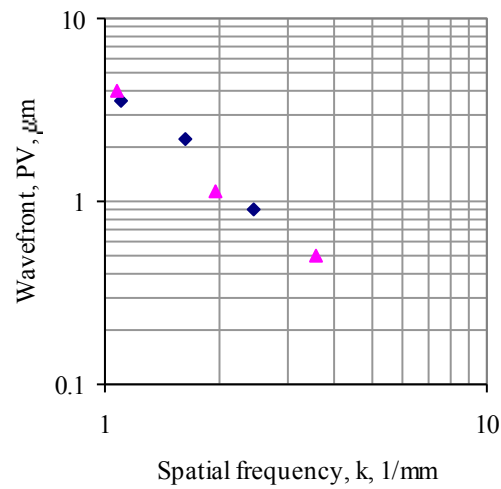


Figure 11. Spatial frequency response function for transparent electrode membrane device. Data for spatially varying wavefront patterns in one dimension, diamonds, and two dimensions, triangles, are further illustrated in Figures 3-6 below. Transparent electrode voltage was approximately 12 V for these data.

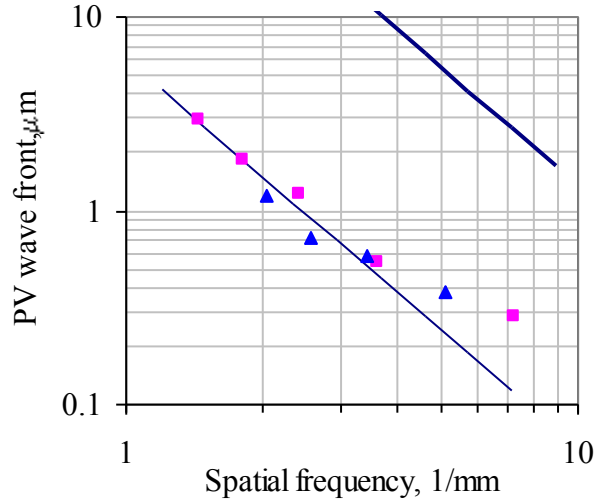


Figure 12. Spatial frequency response for small 256 membrane device (without transparent electrode). For comparison with Figure 1. Measurements from 1D stripe, square data points, and 2D checkerboard, triangle data points, electrode voltage patterns are compared to the model, thin line. Model parameters are  $V=21$  V,  $d_0=18$   $\mu\text{m}$ , membrane stress=5 MPa, thickness = 1  $\mu\text{m}$ . The upper, thick line illustrates the predicted amplitude response for a transparent electrode device operated at 100 V.

## 5. DISCUSSION

A transparent electrode membrane device is considered to be a membrane that is supported only at its periphery and is suspended midway between two electrode planes. The membrane is actuated by means of voltages applied to either electrode plane, that cause the membrane surface to deform.

The static equilibrium of the membrane may be analyzed by considering the total electrostatic + mechanical energy of the system. The electrostatic contribution to the energy is found by considering the membrane as a parallel plate capacitor with each electrode plane. This contribution to the energy is minimized when the membrane snaps down to one or other electrode plane. In a perfectly symmetric case (gap distances and voltages on each electrode plane are equal), the un-deformed, central, membrane position is an unstable equilibrium. Any small deformation toward either electrode results in a net electrostatic force pulling the membrane toward the closer electrode plane.

The mechanical contribution to the energy is found by considering only the tension in the membrane, which acts parallel to the surface of the membrane. The tension acts as a restoring force to the membrane that prevents electrostatic induced snap down under certain conditions. Tension acts to pull the membrane flat, and increasing the tension makes the membrane harder to deform for a given arrangement of voltages applied to the electrodes.

By assuming that voltages applied to either electrode are uniform over the surface of the electrode, and therefore the resulting membrane deformation is parabolic, analytic expressions for the two contributions to the energy may be solved in terms of the relevant device parameters. The resulting expression for the energy can then be used to analyze the device behavior, especially in terms of stability of the central equilibrium position.

## **2. Calculation of the Energy**

Let the shape of the wavefront be described by a function,  $\xi$ , of coordinates in the plane of the membrane such that  $\xi$  is positive for deflections toward the upper electrode in Figure 1. The membrane is constrained at its periphery, therefore  $\xi(r=R)=0$ . Under the influence of electrostatic attraction to either electrode alone, and for small deflections relative to the gap distances, the membrane will deform to a parabolic shape

$$\xi \propto \frac{x}{R}(r^2 - R^2) \quad [1]$$

where  $x$  is defined as the peak deflection,  $x=\xi(r=0)$ .

For large deflections the membrane shape will not in general be parabolic due to single voltages applied to either electrode.\* In the present discussion, the stability of the equilibrium at the undeformed membrane position is being investigated. As a result, only the behavior of the membrane for small deflections is of interest, and then only to ascertain stability. Therefore a parabolic deflection is assumed. In the calculation below, the energy is expressed in terms of the peak deflection of this parabola.

---

\* The membrane shape is determined by the nonlinear Poisson equation, which may admit parabolic solutions for some combination of electrode voltages on the array and transparent electrode.



The electrostatic energy is found from integrating the volume energy density of the electrostatic field,  $E$ , on either side of the membrane, and is given by

$$U_{el} = \int \frac{1}{2} \epsilon_0 E_I^2 dV_I + \int \frac{1}{2} \epsilon_0 E_{II}^2 dV_{II} \quad [2]$$

where region I and region II are defined in Figure 1. The electric fields are given by

$$E_I = \frac{V_{TM}}{(d_T + \xi)} \quad E_{II} = \frac{V_{OM}}{(d_0 - \xi)} \quad [3 \text{ a,b}]$$

Inserting Equation [3a] and Equation [1] into the first term of the electrostatic energy given by Equation [2] and performing the integration gives

$$U_{el_I} = \frac{1}{2} \pi \epsilon_0 R^2 V_{TM}^2 \frac{1}{x} \ln \left| \frac{d_T}{d_T - x} \right| \quad [4]$$

From symmetry, a similar equation expresses the electrostatic energy in region II.

$$U_{el_{II}} = -\frac{1}{2} \pi \epsilon_0 R^2 V_{AM}^2 \frac{1}{x} \ln \left| \frac{d_0}{d_0 + x} \right| \quad [5]$$

Combining Equations [4] and [5] yields the total electrostatic energy of the membrane system.

The mechanical energy is found from integrating the square of the gradient of the membrane shape, and is given by

$$U_{mech} = T \iint |\nabla \xi|^2 dS \quad [6]$$

where the membrane tension is denoted by  $T$ , and the integration is carried out over the membrane surface, and computed in polar coordinates.\* With the membrane shape given by Equation [1], the integral can be carried out to yield

$$U_{mech} = 2\pi T x^2 \quad [7]$$

Thus Equations [4], [5], [7] can be combined to yield the total electrostatic and mechanical energy as a function of the peak displacement,  $x$ , and geometrical and device parameters.

This expression for the energy has been programmed into an Excel spreadsheet in order to explore the effects on the energy, and in particular the stability of the equilibrium at  $x=0$ , of various values of the device parameters. Some results are indicated in the figures below.

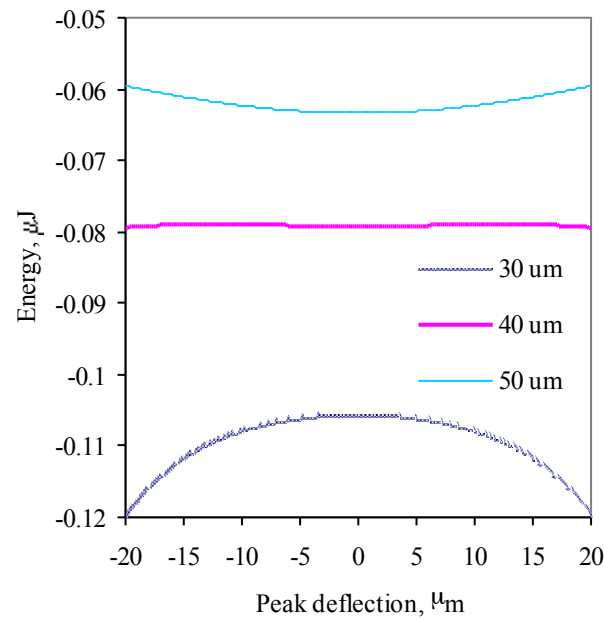


Figure 2. Total energy vs. peak deflection of membrane devices at various gap distances. For these computations a symmetrical device is assumed, i.e.  $d_0=d_T$ . Upper, thin solid curve, illustrates the energy for a membrane with 50  $\mu\text{m}$  electrode-membrane separation. Middle, thick

---

\* In the absence of electrostatic effects, the Lagrange's principle applied to this expression for the energy yields the

solid curve, and lower, stipled curve, illustrate the energy for a 40  $\mu\text{m}$  and 30  $\mu\text{m}$  electrode-membrane separation, respectively. The top two curves have stable equilibria at the origin. Simulated membranes are silicon, 15 mm diameter, 3 MPa stress, operated at 45 V.

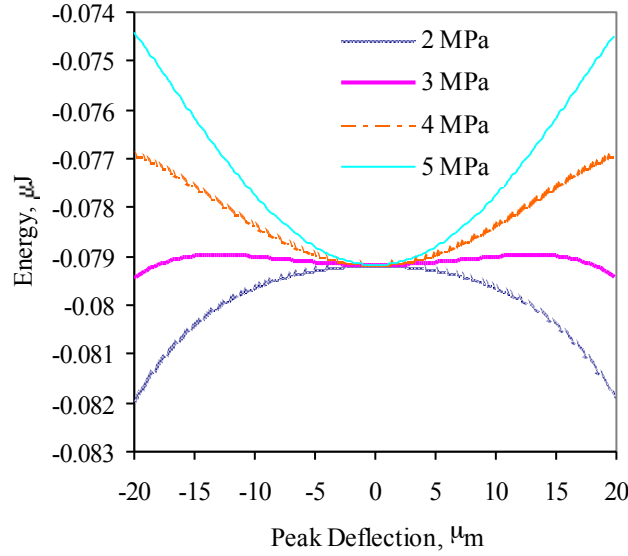


Figure 3. Total energy vs. peak deflection of membrane devices for various values of membrane stress. Upper, thin solid curve, illustrates the energy for membranes with 5 MPa stress. Upper middle, thin dashed curve, and lower middle, thick solid curve illustrate the energy for 4 MPa and 3 MPa stress membranes, respectively. Lower, stipled curve, illustrates the energy for 2 MPa stress membranes. The bottom curve is an unstable equilibrium at zero deflection. Simulated membranes are silicon, 15 mm diameter, 40  $\mu\text{m}$  membrane-electrode gap distance, operated at 45 V. For these computations a symmetrical device is assumed, i.e.  $d_0 = d_T$ .

---

equation of equilibrium, which is well known to be the Laplace equation.

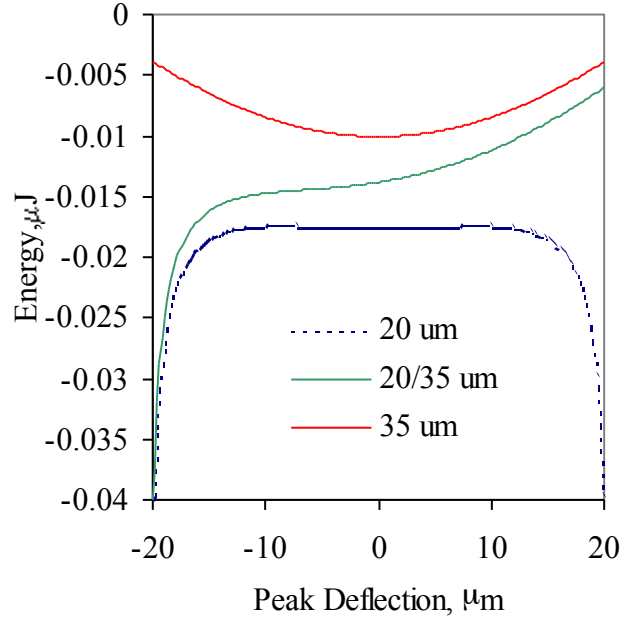


Figure 4. Total energy vs. peak deflection for symmetric and asymmetric gap distances. Upper curve (solid line) illustrates total energy for device with symmetric, 35  $\mu\text{m}$  gap distances; this curve is a stable equilibrium at zero peak deflection. Middle curve illustrates the energy for 20  $\mu\text{m}$  gap distance between membrane and lower electrode and 35  $\mu\text{m}$  gap distance between membrane and upper electrode. The middle curve does not exhibit an equilibrium at zero peak deflection. The bottom curve illustrates the energy for symmetric 20  $\mu\text{m}$  gap distances. The equilibrium at zero peak deflection is effectively neutral.

The stability of the membrane is determined by nature of the energy as a function of the peak deflection. Combinations of device parameters that yield a stable equilibrium at zero values of

peak deflection can be expected to yield stable devices. In contrast, devices with parameters that lead to an unstable or neutral equilibrium at zero values of peak deflection will be difficult to control.

These computations show that the energy is sensitively dependent on the stress and membrane-electrode gap distances, and therefore these parameters have an important impact on the design of devices.

Laboratory experiments with device 11-17-204-A suggest that above  $V_T \sim 12$  V (transparent electrode voltage) the membrane becomes difficult to control. This may be an indication of the device becoming energetically unstable at zero peak deflection.

## 6. CONCLUSION

## APPENDIX

Actuator signals,  $x$ , (e.g. voltages) are related to wavefront sensor measurements,  $b$ , according to a matrix equation, which relates the  $N$  actuators to the  $M$  wavefront sensor measurements as:

$$A \cdot x = b \quad [1]$$

where  $b$  is an  $M \times 1$  array of wavefront measurements,  $A$  is an  $M \times N$  matrix,  $x$  is an  $N \times 1$  array of actuator drive values (e.g. voltages).

The "standard problem" of wavefront correction consists of inverting the matrix  $A$  in [1] in order to compute the desired actuator drives,  $x$ , from the known wavefront measurements,  $b$ :

$$x = A^{-1} \cdot b \quad [2]$$

Because the system is generally overdetermined,  $M > N$ , a least squares pseudo-inverse is obtained, which is given by:

$$A^{-1} \sim (A^T A)^{-1} A^T \quad [3]$$

where  $A^T$  is the transpose of  $A$ . Note that  $(A^T A)$  is a square matrix that can be inverted using standard techniques.

Using component form for the vectors  $x$ ,  $b$  and matrix  $A$ , the quantity

$$X^2 = \sum_{i=1}^M \left( x_i - \sum_{k=1}^N b_k A_{ik} \right)^2 \quad [4]$$

is minimized by the particular vector  $x$  which is given by:

$$x = (A^T A)^{-1} A^T \cdot b \quad [5]$$

Hence the problem is solved, in a least squares sense, by Equation [5].

The pseudo inverse of  $A$ , given by [3], is termed the reconstructor for the system. It must be computed before closed loop operations are initiated. The reconstructor is found by a two step process.

First, the matrix  $A$  is determined by applying a unit voltage to each actuator in turn, and measuring the resulting wavefront. In this manner, each measurement determines one column of the matrix  $A$ . The resulting reconstructor is called a "poke reconstructor." Second, the pseudo inverse of  $A$ , i.e. the reconstructor,  $R$ , is calculated:

$$R \equiv A^{-1} \sim (A^T A)^{-1} A^T \quad [6]$$

The square matrix in ( ) is difficult to invert, and therefore singular value decomposition is used. Inspection and/or elimination of anomalously low singular values improves the results.

The control loop of the system is a simple integrator, which computes the new actuator drive



signals,  $x_{n+1}$  at each iteration,  $n$ , from the previous drive signals,  $x_n$ , and a correction term according to

$$x_{n+1} = x_n + gR \cdot b \quad [7]$$

where  $R$  is the Reconstructor matrix given by [6],  $b$  is the array of wavefront sensor measurements taken during the control loop iteration, and  $g$  is an adjustable gain.

## ACKNOWLEDGEMENTS

The authors are grateful for support and assistance from many members of the MEMS research group at Lucent Technologies Bell Laboratories and the New Jersey Nanotechnology Center. In particular, we thank Flavio Pardo and Alex Tran for assistance in layout and design, C. S. Pai for supplying SOI wafers and for discussions, Ray Cirelli, Ed Ferry, Fred Klemens for their efforts during fabrication, Arman Gasparyan, Martin Haueis and Herb Shea for conversations and other contributions to laboratory testing, and Rich George and Bob Frahm for wire bonding. We thank Walter Brown and Linda Sauter for resonant frequency measurements. For conversations about membrane strain and for suggesting the origin of astigmatism strain of the membranes, we thank Dennis Mansell of Intellite Corporation. This work has been supported by the National Science Foundation Science and Technology Center for Adaptive Optics, managed by the University of California at Santa Cruz under cooperative agreement No. AST – 9876783.

1. R. E. Aldrich, "Deformable Mirror Wavefront Correctors," in *Adaptive Optics Engineering Handbook*, R. K. Tyson, ed. (Marcel Dekker, Inc., New York, 2000), pp. 151-197. See also other articles in the same volume.
2. G. Vdovin, and P. M. Sarro, "Flexible mirror micromachined in silicon," *Applied Optics* 34, 2968-2972 (1995).
3. L. Zhu, P-C Sun, D-U Bartsch, W. R. Freeman, Y. Fainman, "Adaptive control of a micromachined continuous-membrane deformable mirror for aberration compensation," *Applied Optics* 38, 168-178 (1999).
4. I. Iglesias and P. Artal, "Closed loop adaptive optics in the human eye," *Optics Letters* 26, 746-748 (2001).
5. L. Zhu, P-C Sun, D-U Bartsch, W. R. Freeman, Y. Fainman, "Wave-front generation of Zernike polynomial modes with a micromachined membrane deformable mirror," *Applied Optics* 38, 6019-6026 (1999).
6. C. Paterson, I. Munro and J. C. Dainty, "A low cost adaptive optics system using a membrane mirror," *Optics Express* 6, 175-185 (2000).
7. R. K. Tyson and B. W. Frazier, "Microelectromechanical system programmable aberration generator for adaptive optics," *Applied Optics* 38, 168-178 (1999).
8. O. Albert, L. Sherman, G. Mourou, T. B. Norris, G. Vdovin, "Smart microscope: an adaptive optics learning system for aberration correction in multiphoton confocal microscopy," *Optics Letters* 25, 52-54 (2000).
9. G. Vdovin and V. Kiyko, "Intracavity control of a 200-W continuous-wave Nd:YAG laser by a micromachined deformable mirror," *Optics Letters* 26, 798-800 (2001).

10. H. M. Dyson, R. M. Sharples, N. A. Dipper, G. V. Vdovin, "Cryogenic wavefront correction using membrane deformable mirrors," *Optics Express* 8, 17-26 (2001).

# FIGURES

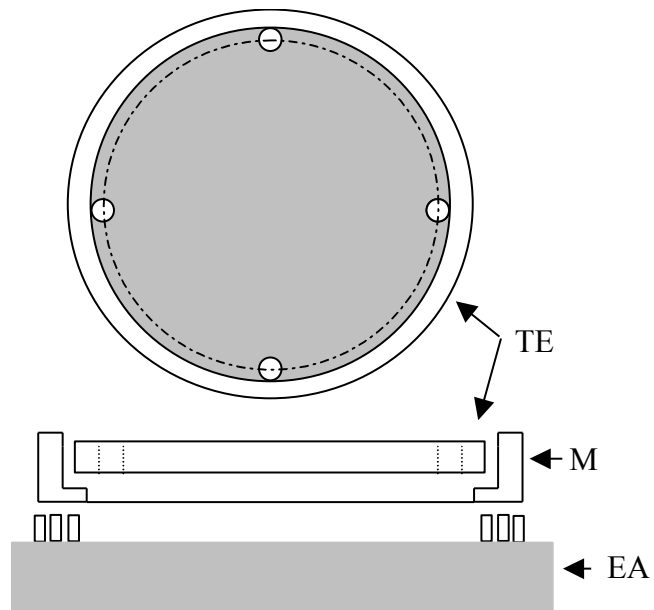


Figure 1

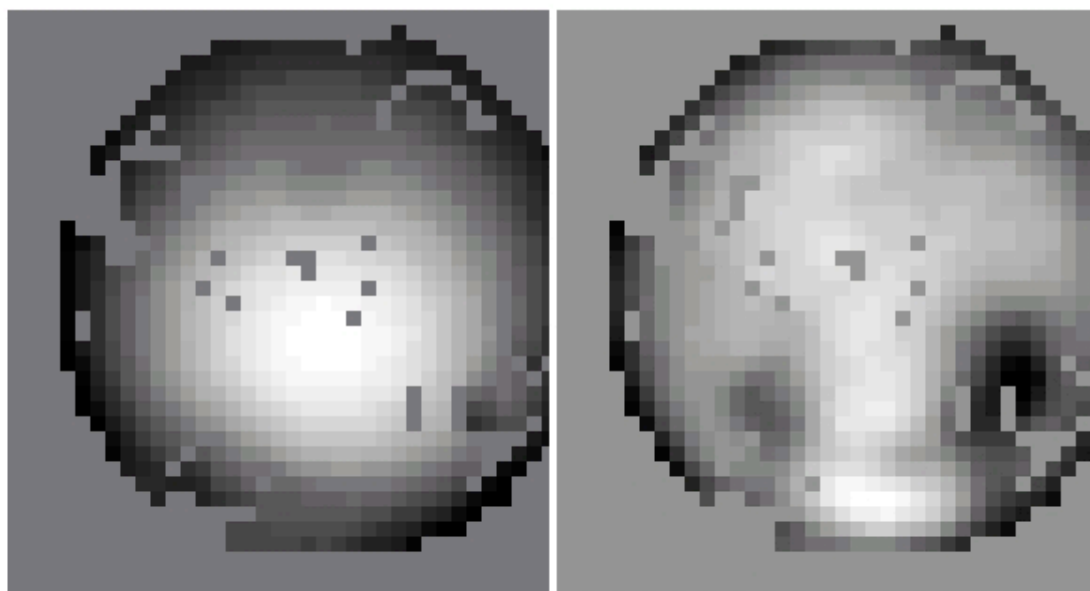


Figure 2

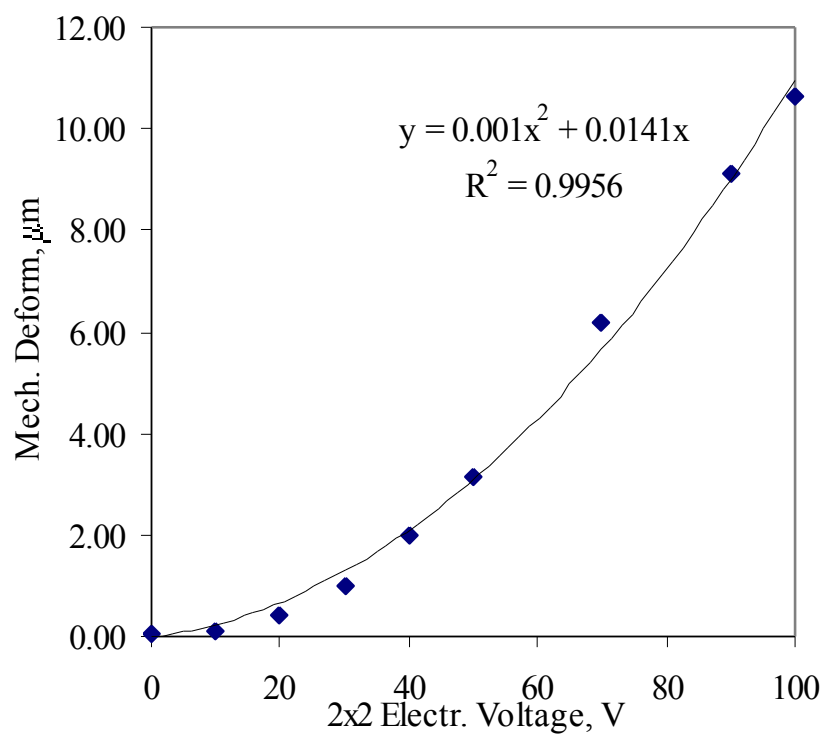


Figure 3#

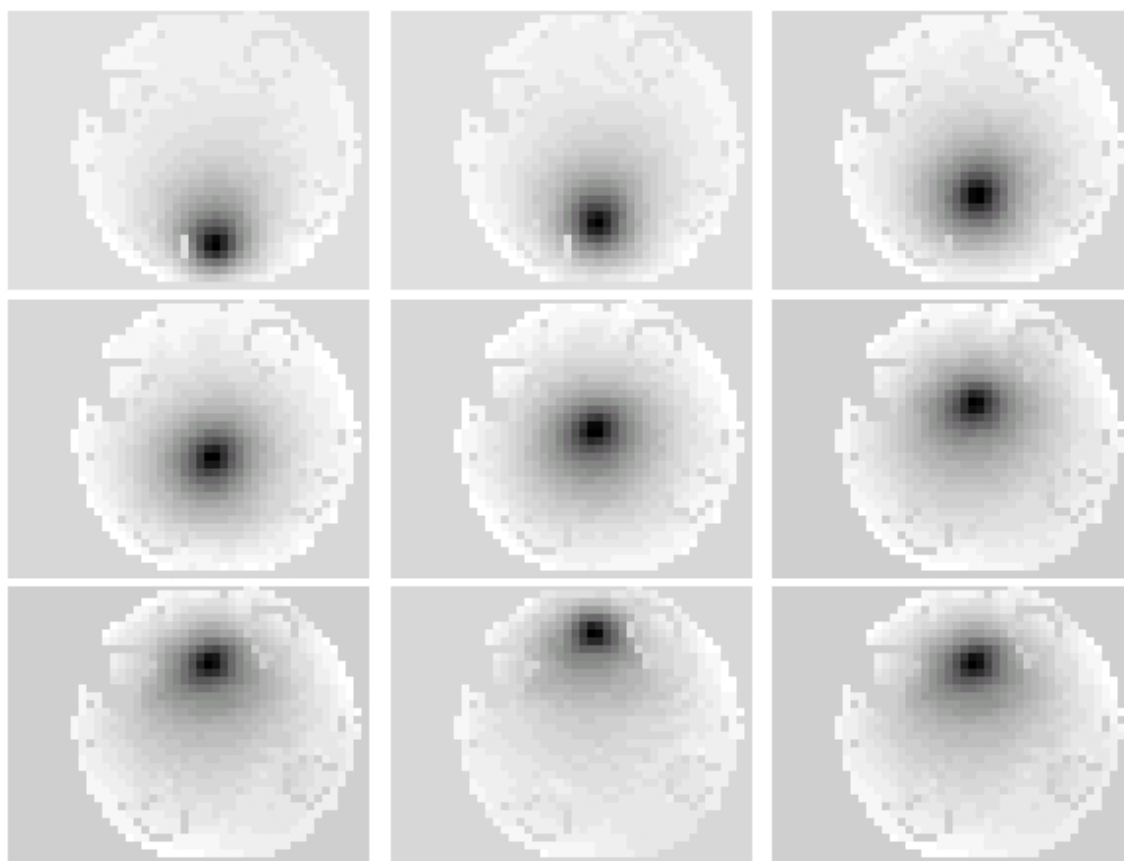


Figure 3\*

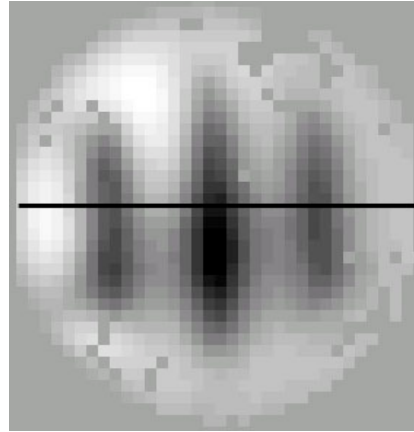
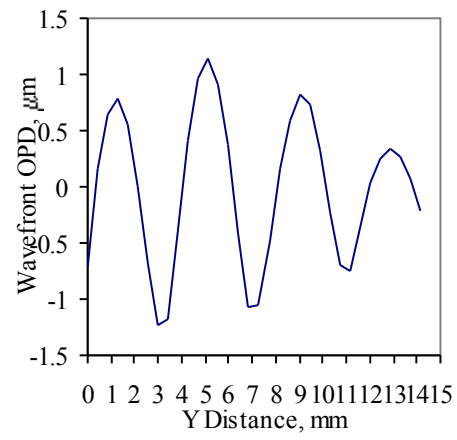


Figure 3\$ a,b



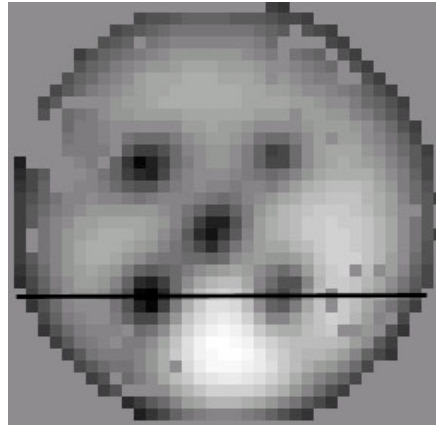
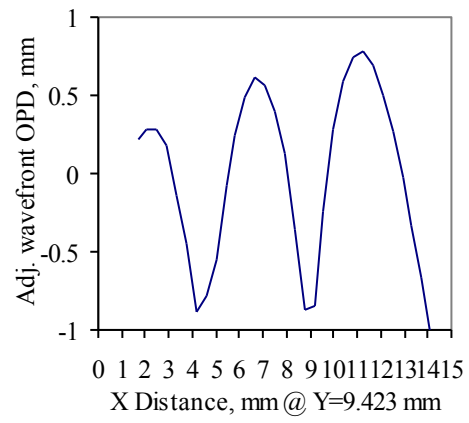


Figure 3% a,b

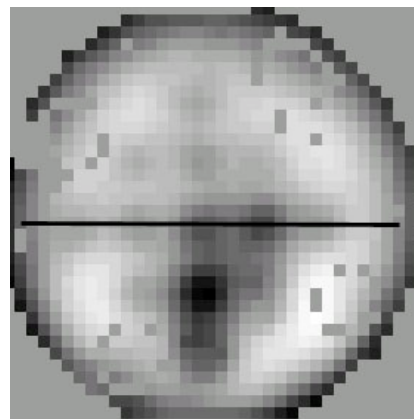
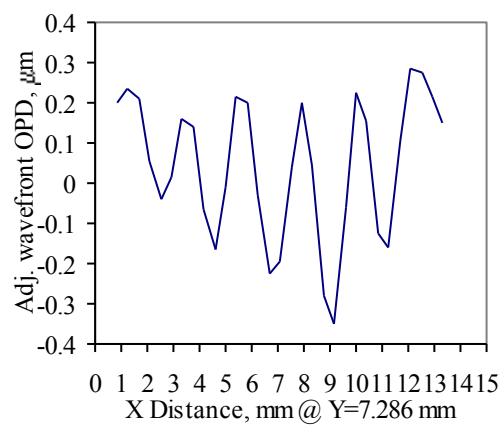


Figure 3& a,b

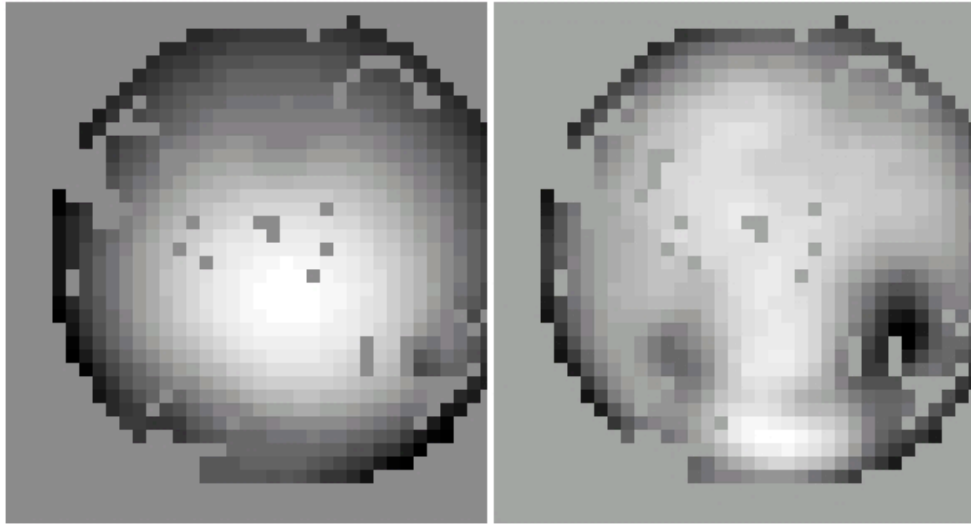


Figure 3 a,b.

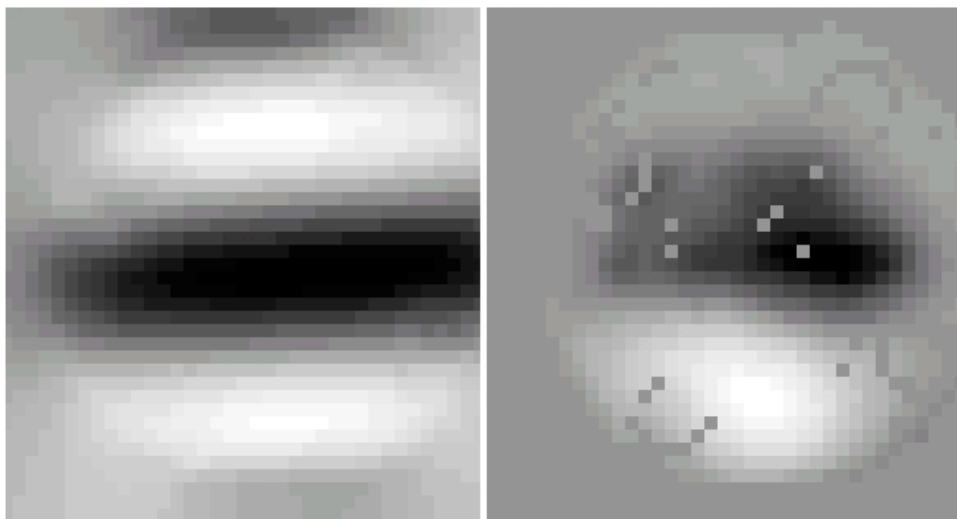


Figure 4 a,b.

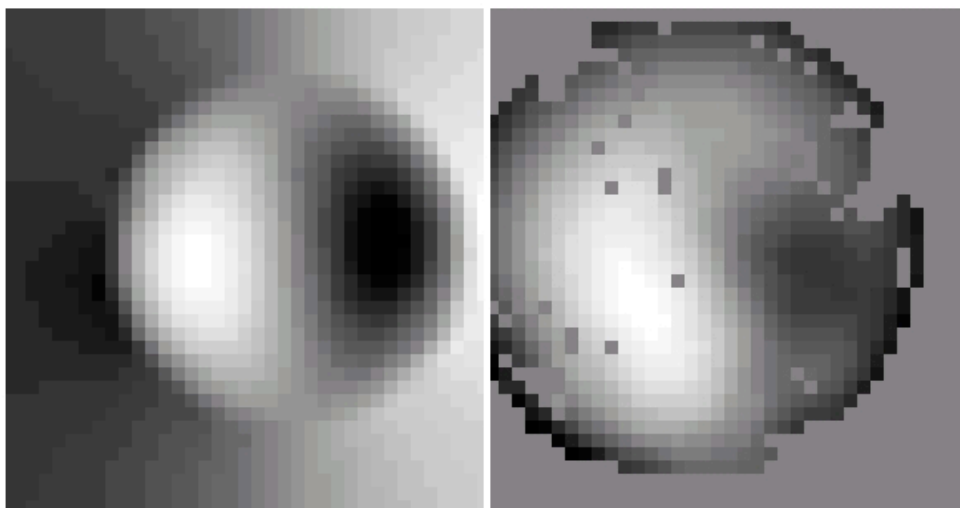


Figure 5 a,b

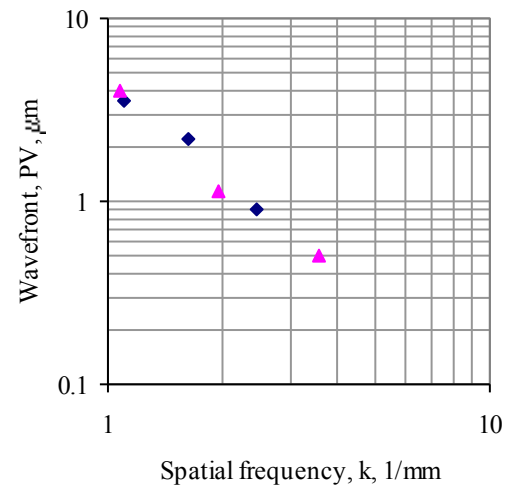


Figure 11.

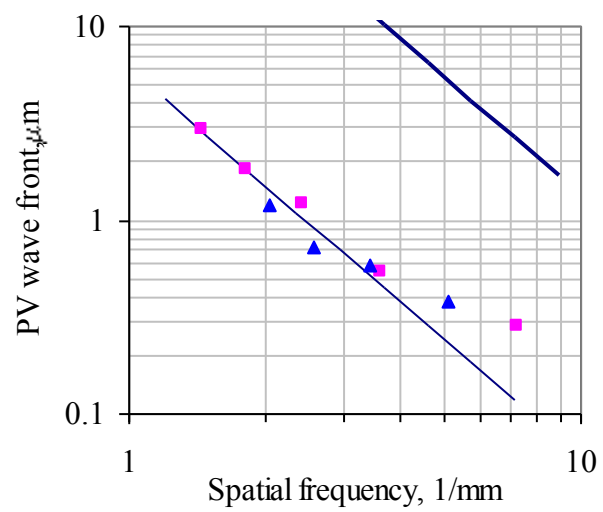


Figure 12

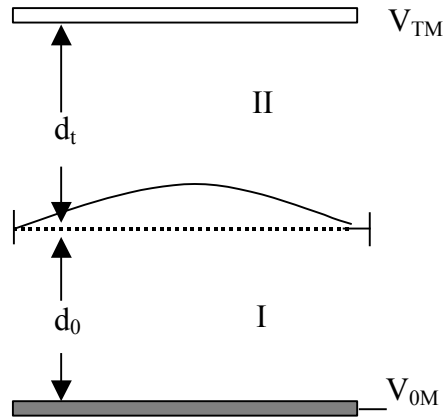


Figure 9

#### FIGURE CAPTIONS

Figure 1. Schematic drawing of transparent electrode membrane device. The upper diagram illustrates a top view of the 16 mm diameter, circular transparent electrode. Indium tin oxide coating, applied to the underside of the part, is shown in gray. Vent holes around the periphery allow air passage through the assembled device to mitigate squeeze film damping. The bottom diagram illustrates the completed device in cross section. The transparent electrode, labeled TE, fits into the micro-fabricated cavity within the membrane chip, labeled M, and is supported 30-60  $\mu\text{m}$  above the membrane; the membrane is supported 20-40  $\mu\text{m}$  above the 1024 electrode array, labeled EA, by polyimide posts. Figure not to scale.



Figure 2 a,b. Before and after command to flat experiment. Left figure (a) illustrates measured wavefront resulting from 9 V applied to the transparent electrode. PV OPD is 19  $\mu\text{m}$ .

Wavefront shape is an off-center paraboloid. Right figure (b) illustrates measured wavefront resulting from closing the loop and iterating to a flat wavefront. PV OPD is 4  $\mu\text{m}$ . “West” chip side is down in the figure. “North” is to the left. Data taken on 1/13/2005.

Figure 3#. Deflection vs. voltage data for the membrane device operated in a 2x2 binning mode. Data points (diamonds) consist of mechanical deflections at each voltage. Mechanical deflection was inferred from the wavefront optical path difference measurements by dividing the peak to valley optical path difference for each measurement by two (due to double pass reflection). The solid line is a quadratic fit to the data, with the fit constrained to pass through the origin. The equation of the best fit line and  $R^2$  goodness of fit statistic are indicated in the figure.

Figure 3% a,b. Left figure (a) illustrates a slice through the wavefront optical path difference data used in a 2D spatial variation pattern. A linear trend has been removed from the data for clarity. Right figure (b) illustrates the entire optical path difference data. The horizontal black line corresponds to the position of the slice through the data depicted in (a). For these data, five 2x2 electrode bins were charged to 90 V (corresponding in position to the dark spots in the figure), and the transparent electrode was charged to 13 V. Peak to valley optical path difference over the entire wavefront is 9.6  $\mu\text{m}$ .

Figure 3& a,b. Left figure (a) illustrates a slice through the wavefront optical path difference data used in a 2D spatial variation pattern. A moving average trend has been removed from the data for clarity. Right figure (b) illustrates the entire optical path difference data. The horizontal black line corresponds to the position of the slice through the data depicted in (a). For these data, 13 4x4 electrode bins were charged to 44 V (corresponding in position to the dark spots in the figure), and the transparent electrode was charged to 13 V. Peak to valley optical path difference over the entire wavefront is 10.8  $\mu\text{m}$ .

Figure 3\*. Representative influence functions of 1024 electrode membrane device. Each image illustrates the wavefront (optical path difference) resulting from energizing a single electrode of the array. The dark spot corresponds to a (peak to valley) deformation of 9  $\mu\text{m}$ . Operating voltage was 120 V.

Figure 3\$ a,b. Left figure (a) illustrates a slice through the wavefront optical path difference data used in a 1D spatial variation pattern. An overall parabolic trend has been removed from the data for clarity. Right figure (b) illustrates the entire optical path difference data. The horizontal black line corresponds to the position of the slice through the data depicted in (a). For these data, three rows of electrodes were charged to 5, 18, 31 V respectively (corresponding in position to the vertical stripes in the figure), and the transparent electrode was charged to 11 V. Peak to valley optical path difference over the entire wavefront is 9.6  $\mu\text{m}$ .

Figure 3 a,b. Before and after command to flat experiment. Left figure (a) illustrates measured wavefront resulting from 9 V applied to the transparent electrode. PV OPD is 19  $\mu\text{m}$ . Wavefront shape is an off-center paraboloid. Right figure (b) illustrates measured wavefront resulting from closing the loop and iterating to a flat wavefront. PV OPD is 4  $\mu\text{m}$ . “West” chip side is down in the figure. “North” is to the left. Data taken on 1/13/2005.

Figure 4 a,b. Left figure (a) illustrates a target wavefront for generation by the deformable mirror. Right figure (b) illustrates the measured wavefront after iterating to the target wavefront in (a). Peak to valley optical path difference of the measured wavefront is approximately 7  $\mu\text{m}$ . Data taken 01/10/2004

Figure 5 a,b. Left figure (a) illustrates target wavefront, the Zernike polynomial  $Z_6$ . Target wavefront PV OPD is approximately 6  $\mu\text{m}$ . The right figure (b) illustrates the wavefront OPD after iteration to the desired wavefront shape. Measured PV wavefront deformation is 13  $\mu\text{m}$ . Right image has been inverted for comparison with the target wavefront.

Figure 9. Schematic diagram of a membrane mirror device. The membrane, solid line, is located between top, transparent electrode and bottom, actuating electrode. The membrane experiences deformations relative to the flat position (dashed line) in response to electric fields in regions I

and II. Voltages refer to the relative voltage between the respective electrode plane and the membrane, which may be at ground or at some non-zero voltage.

Figure 11. Spatial frequency response function for transparent electrode membrane device. Data for spatially varying wavefront patterns in one dimension, diamonds, and two dimensions, triangles, are further illustrated in Figures 3-6 below. Transparent electrode voltage was approximately 12 V for these data.

Figure 12. Spatial frequency response for small 256 membrane device (without transparent electrode). For comparison with Figure 1. Measurements from 1D stripe, square data points, and 2D checkerboard, triangle data points, electrode voltage patterns are compared to the model, thin line. Model parameters are  $V=21$  V,  $d_0=18$   $\mu\text{m}$ , membrane stress=5 MPa, thickness = 1  $\mu\text{m}$ . The upper, thick line illustrates the predicted amplitude response for a transparent electrode device operated at 100 V.

## TABLES

Electrode binning	# binned electrodes in array (modes)	Effective electrode width, $\mu\text{m}$	Voltage reqd. for 10 $\mu\text{m}$ (optical) deflection, V
1x1	1024	275	>~120
2x2	361	550	71
3x3	169	825	40
5x5	63	1375	25
7x7	36	1925	19
16x16	9	4400	10

Table 1

## TABLE CAPTIONS

Table 1. Binning modes of 1024 membrane mirror and operating voltage required for 10  $\mu\text{m}$  (optical) wavefront deformation. First column indicates the number of electrodes per bin; the second column indicates the number of binned electrodes in the entire array; third column indicates the width of each electrode bin; fourth column indicates the voltage required on a single binned electrode to yield 10  $\mu\text{m}$  peak to valley wavefront deformation, with all other array voltages and transparent electrode voltage held at zero volts. In each case of single binned electrode actuation, the resulting wavefront deformation had a FWHM of approximately 3 mm.